

Liquid-phase catalytic growth of graphene

Pin Tian

Yunnan University

Libin Tang (✉ sscitang@163.com)

Kunming Institute of Physics

Jinzhong Xiang

Yunnan University

Shu Ping Lau

The Hong Kong Polytechnic University <https://orcid.org/0000-0002-5315-8472>

Shouzhong Yuan

Kunming Institute of Physics

Dengquan Yang

Kunming Institute of Physics

Lain-Jong Li

University of New South Wales

Kar Teng

Swansea University

Article

Keywords: graphene, energy storage, catalysis

Posted Date: May 26th, 2021

DOI: <https://doi.org/10.21203/rs.3.rs-536945/v1>

License: © ⓘ This work is licensed under a Creative Commons Attribution 4.0 International License.

[Read Full License](#)

Version of Record: A version of this preprint was published at Journal of Materials Chemistry C on January 1st, 2021. See the published version at <https://doi.org/10.1039/D1TC04187H>.

Abstract

Ability to mass produce graphene at low cost is of paramount importance in bringing graphene based technologies into market. Here we report a facile liquid-phase catalytic growth of graphene suitable for mass production. Iodine tincture is used to catalyze graphene quantum dots to form graphene films at room temperature. Such method has many advantages, such as environment friendly, high yield, low cost and wide choice of substrates. Furthermore, bandgap of the graphene films is tunable by post-annealing. A photodetector based on the graphene films was developed and could response to a broad wavelength between 365 and 1200 nm. It exhibited detectivity and responsivity of up to $1.1 \times 10^{13} \text{ cmHz}^{1/2} \text{ W}^{-1}$ and 81.3 mA W^{-1} respectively. Hence, the graphene films demonstrated significant applications in the field of optoelectronics. Interestingly, surface of the graphene film prepared by this method has wrinkles that can also be explored for energy storage applications.

Introduction

Graphene, a pioneer of two-dimensional materials, has attracted great scientific interests due to its excellent physical and chemical properties since its discovery by Andre Geim's group¹. An extensive research on the properties of the material has led to many novel applications, such as flexible devices²⁻⁶, transparent electrodes⁷⁻¹³, ultra-fast photodetectors¹⁴⁻¹⁷ and wearable temperature sensors¹⁸⁻²⁰ by taking advantage of graphene's high transmittance (e.g. visible light transmittance of 97.7%²¹), flexibility, conductivity (e.g. high carrier mobility of $2.5 \times 10^5 \text{ cm}^2 \text{ V}^{-1} \text{ s}^{-1}$ ²² at room temperature) and thermal conductivity (of 3000 W m K^{-1} ²³). Also, the magnetic property of graphene has led to the development of unique filter membrane^{24,25}. Other applications include high performance energy storage²⁶⁻³⁰ by utilizing the surface wrinkles of graphene. Although there are many reports on the novel applications of graphene, most of these developments remain in research laboratories and have not reached the mass market due to inability to mass produce graphene at low cost. Therefore, there is an urgent need to develop a preparation technique that is suitable for low cost mass production of graphene in order to bring graphene based technologies to the mass market. At present, there are several mainstream techniques to produce graphene, such as mechanical stripping methods^{31,32}, chemical vapor deposition methods³³⁻³⁶, epitaxial growth methods³⁷⁻³⁹, liquid stripping methods or redox methods⁴⁰⁻⁴², and molecular self-assembly methods⁴³⁻⁴⁶. Each of these methods has advantages and disadvantages, for example, graphene prepared by mechanical stripping exhibits the best material quality and device performances however this method is only suitable for laboratory research due to its low yield. The conventional metal-catalyzed chemical vapor deposition method is also extremely low in yield due to the complex preparation processes, especially the transfer process. More recently, various chemical vapor deposition methods have been developed, such as metal-catalyst-free chemical vapor deposition⁴⁷ and plasma enhanced chemical vapor deposition^{48,49}, to avoid detrimental defects caused by the transfer process in the conventional metal-catalyzed chemical vapor deposition methods. However, graphene produced by these methods exhibits significantly reduced performances due to imperfect nucleation and absence of

catalytic reaction. The current solution based processing techniques, such as liquid phase stripping and redox methods, can produce graphene films easily and at very high yield, but they require the use of strong acids and alkali as well as highly toxic and explosive chemicals, which are very harmful to the environment. Hence, these methods are unsuitable for industrial production of graphene for environmental reasons. The molecular self-assembly method is considered current state of the art technology due to facile, high-yield and scalable synthesis process⁵⁰ but it is limited by the choice of precursors that are required to meet a series of thermodynamic, kinetic, and structural criteria imposed by the dimensions and symmetry, the nature of the surface used as growth substrate, and technical limitations imposed by the UHV system used in fabrication⁵¹, hence resulting in high production cost of graphene.

Here we developed a facile liquid-phase catalysis method to produce graphene. Fig. 1a illustrates the entire process. Firstly, graphene quantum dots (GQDs) are prepared using sucrose as precursor. They are then catalyzed into graphene films using iodine as catalyst. Unlike conventional catalyst-based chemical vapor deposition method that requires elevated temperature to prepare graphene films⁵², the liquid-phase catalysis method using iodine as catalyst can rapidly produce graphene at ambient temperature. Hence, this method has many advantages, such as environment friendly, low cost, high yield, simple and rapid preparation process, low energy consumption, and wide choice of substrates. Importantly, this method is highly suitable for mass production of graphene at low cost, which will expedite the commercialization of graphene based technologies. Furthermore, the method can be explored to prepare other two-dimensional materials. In this work, a photodetector was developed using graphene films prepared by the liquid-phase catalysis method. Characterization of the device suggests that the absorption layer at the photodetector was formed by multilayer graphene stacking. This is different from the orderly stacking graphite, which cannot be used in optoelectronic devices due to coupling of interlayer charge. The photodetector could response to a broad wavelength range between 365 and 1200 nm, with detectivity (D^*) of up to 1.1×10^{13} cmHz^{1/2}W⁻¹ and responsivity of up to 81.3 mA W⁻¹. Therefore, these graphene films prepared by the liquid-phase catalysis method can find applications in the field of optoelectronics, such as photodetectors, solar cells and light-emitting diodes, as well as in other fields, such as energy storage, due to their interesting surface morphology.

Results

Liquid-phase catalysis and characterization of graphene

Fig. 1a shows a schematic diagram of the liquid-phase catalytic growth process of graphene.

Colorless sucrose solution was caramelized at 200°C to form GQDs, which turned the solution into a yellow viscous liquid. Subsequently, the viscous liquid was diluted with a mixed solvent of alcohol and deionized water. Iodine was then introduced into the GQDs solution and turned the color of the solution from yellow to dark brown, as shown in right inset of Fig. 1a. Details on the preparation process can be found in Methods section. TEM characterization on the yellow solution showed high density and even

distribution of GQDs, as shown in Supplementary Fig. 1a and b. The size of these quantum dots was 3.13 nm as shown in Fig. 1k. High-resolution TEM (HRTEM) image in Fig. 1b-d revealed circular shape of the as-grown GQDs. Supplementary Figs. 2a and b show the lattice fringes of the dots with spacing of 0.214 nm and 0.246 nm respectively, which is characteristic spacing of graphene. After the introduction of iodine, the GQDs rapidly grew in size from a few nanometers to hundreds of nanometers and into graphene flakes as shown in HRTEM image of Fig. 1e-g. Interestingly, there were wrinkles at the graphene prepared by the liquid-phase catalysis method as shown in Supplementary Fig. 1d. Lattice fringes from region \square and \square of the HRTEM image in Supplementary Fig. 1d are shown in Supplementary Figs. 2c and d, which has lattice spacing of 0.214 nm in-plane and 0.361 nm in c-axis direction respectively. This revealed good crystallinity of graphene. Selective area electron diffraction (SAED) was performed at the blue dotted circle region in Supplementary Fig. 1c, which showed hexagonal diffraction pattern of graphene (Supplementary Fig. 2e). Furthermore, the FFT patterns of Fig. 1e-g showed perfect hexagonal structures, as shown in Fig. 1h-j respectively. Hence, these results again indicated good crystallinity of graphene prepared by this method. Interestingly, the statistical size of graphene flakes was up to 275.78 nm, as shown in Fig. 1k. There were evidences that the size of some graphene flakes could reach micron scale as shown in Fig. 2a. This implies that the liquid-phase catalysis method is capable of mass producing high quality graphene with size ranging from hundreds of nanometers to micron scale. EDS measurements (Supplementary Fig. 1e) showed high concentration of iodine element on the graphene, suggesting that the iodine remained in the solution and attached to the graphene after completion of the catalytic growth. Fig 2b shows a HRTEM image of region \square in Fig. 2a. It showed that multi-layered graphene was produced in the solution using the liquid-phase catalysis method. Besides, the interlayer spacing of 0.365 nm, as measured in Fig. 2c, indicates that the graphene produced using this method is constructed by layer-by-layer stacking. SAED were performed (as shown in Fig. 2d) to investigate the superposition of the graphene. By measuring the distance (d) between the center spot and the vertices of each hexagonal ring, D (e.g. $D=1/d$) of each lattice face can be calculated. According to the crystal surface spacing of graphite, the corresponding lattice face of each spot was obtained, as shown in Fig. 2d, where $d_1=2.946$ 1/nm, $d_2=4.950$ 1/nm, $d_3=8.620$ 1/nm and $d_4=9.481$ 1/nm corresponding to $D_1=0.339$ nm, $D_2=0.202$ nm, $D_3=0.116$ nm and $D_4=0.105$ nm respectively. Thus, the electron diffraction pattern corresponded to the lattice face⁵³ (002), (101), (112) and (201), which indicate c-axis direction as well as other directions of graphene. This suggests that the graphene flakes were randomly stacked. Also, the TEM images showed that the graphene flakes were not flat but have lots of wrinkles. Therefore, graphene with various morphologies can be grown from GQDs using this method, as illustrated in Fig. 2e.

Modulation of energy bandgap of graphene Intrinsic graphene has zero bandgap, which greatly limits its application, especially in the field of semiconductor. However, the energy bandgap of graphene can be opened up by either doping or controlling its size as demonstrated by others⁵⁴⁻⁵⁶. The graphene solution prepared using the liquid-phase catalysis method was spin-coated on to a substrate due to its good viscosity and then annealed at elevated temperature under vacuum to obtain solid-state graphene films, as shown in Fig. 3a. Using the spin-coating deposition technique, it is possible to produce large area graphene film on any substrate. XPS measurements revealed the absence of iodine at the solid graphene

film (see Supplementary Fig. 3), hence suggesting that the catalyst was removed upon annealing and there was no evidence of iodine doping. The graphene film was homogeneous and has a thickness of 609 nm as measured using AFM (as shown in 3b). Optical absorption characterization was performed on both the solution and the film during the preparation process. The absorption peaks of the GQDs solution were located at 285 nm during the nucleation stage. After the liquid-phase catalysis growth of graphene, the absorption peaks of the graphene solution red-shifted and were located at 353 nm. Moreover, its absorption spectrum was widened, which is a notable feature of graphene. After the annealing treatment, the liquid-phase graphene was solidified into graphene thin film, which led to a significant increase in its absorption intensity by at least three orders of magnitudes (e.g. 2015.9%) from that of the GQDs. A further widening of the absorption spectrum was observed (Fig. 3c), which can be attributed to the removal of moisture and carbon dioxide, thus resulting in a higher order of graphene films (see Supplementary Fig. 4). The optical bandgap of graphene can be calculated from its absorption spectrum since it is a direct bandgap material (see Supplementary Fig. 5 and Supplementary Table 1). Detailed calculation is shown in the Supplementary Discussion. The results showed that the bandgap of the solid graphene films varied significantly at different annealing temperatures, for example, the optical bandgap decreases with increasing annealing temperatures. Hence, the bandgap of liquid-phase catalytic graphene can be modulated by annealing treatment. Based on the overall trend, the bandgap can be tuned from wide bandgap semiconductor (2.2 eV) at 500°C to conductor (0 eV) at sufficiently high temperature (see Fig. 3d). This is an exciting discovery as the graphene prepared by the liquid-phase catalysis method will lead to many novel applications in the semiconductor industry.

Fabrication and characterization of photodetector A simple photodetector structure, shown in Fig. 4a, consisting of the graphene film as an absorbent layer was fabricated. The liquid-phase catalyzed graphene was spin-coated on the surface of ITO film. Fig. 4a illustrates the structure of the graphene films, which comprised of randomly stacked graphene flakes as the absorbent layer. The graphene film was then annealed at 600°C, which is limited by the maximum temperature of the ITO film⁴⁶. An energy band structure of the photodetector with calculated optical bandgap of 1.78 eV is shown in Fig. 4b. Fig. 4c

shows I - V measurements performed on the photodetector under dark and illumination of LEDs with different wavelengths from 365 nm to 940 nm at various power densities (e.g. 365 nm @ 0.18 mWcm⁻², 400 nm @ 0.54 mWcm⁻², 500 nm @ 1.32 mWcm⁻², 555 nm @ 0.95 mWcm⁻², 660 nm @ 2.8 mWcm⁻², 740 nm @ 2.5 mWcm⁻², 850 nm @ 1.4 mWcm⁻², 940 nm @ 0.8 mWcm⁻²). Such measurements demonstrated the capability of the photodetector in detecting wavelength ranging from ultraviolet to infrared. An important figure of merit for a photodetector⁵⁷ is responsivity (R), which can be calculated using the following formula:

$$R = J_{ph}/P_{opt}$$

where J_{ph} is photocurrent, which equals to absolute value of the current density under illumination subtracting that in the dark, and P_{opt} is incident optical power. Another important figure of merit is

detectivity, D^* , which can be expressed as

$$D^* = R /$$

where J_{dark} is dark current density and q is unit charge. Using the I - V characteristics, both R and D^* can be calculated. Curves of R and D^* vs. applied voltage of the photodetector are shown in Supplementary Fig. 6. When applying 1.85V, the photodetector exhibited peak detectivity () and responsivity as shown in Fig. 4d. Under illumination at 365 nm, the detectivity and responsivity were increased to $1.1 \times 10^{13} \text{ cmHz}^{1/2} \text{ W}^{-1}$ and 81.3 mA W^{-1} respectively. Besides, the trend of D^* and R responding to wavelength was similar to that of photocurrent. As shown in Fig. 4e, the photocurrent spectrum revealed a broad response wavelength of the photodetector, which ranged from 400 to 1200 nm. Such broad coverage in the visible and near-infrared range means that the graphene film is invaluable for applications in solar cell, photocatalysis and light-emitting diodes etc. Since the optical bandgap of the graphene film was 1.78 eV, its response wavelength should position at 696.6 nm (e.g. $\lambda_{\text{peak}} = 1240(\text{nm}) / E_g$). The broad response wavelength therefore indicates extraordinary phenomena exhibited by the graphene film. Under the excitation of photons with specific energy, electron-hole pairs are excited inside the graphene. These electrons and holes are separated to Al and ITO electrodes respectively, as shown in Fig 4a. When photons with excessive energy ($\lambda > 365 \text{ nm}$) incident on to the graphene, heat (and/or other forms of energy) is also released, which contributes to the current of the photodetector.

Discussion

Although the specific catalytic mechanism is still unclear, the liquid-phase catalytic growth of graphene has many significant differences comparing to current methods. Firstly, the growth process is safe and environment friendly. Besides, the method is facile and can produce high yield of graphene at room temperature. Furthermore, the solution based method allows easy and rapid production of graphene devices at very low cost. Interestingly, the solid graphene film prepared using this method exhibited different characteristics as compared to conventional graphite, for example, the disordered stacking structure of graphene in the film can prevent electron coupling as observed in graphite, thus enhancing the absorption of graphene film. Importantly, the optical properties of the graphene film can be modified simply by controlling its annealing temperature. Due to ultralow absorption of graphene, the responsivity of graphene photodetectors is usually below 10 mA W^{-1} ^{58,59}. The detectivity of most graphene photodetectors is usually below $10^{12} \text{ cmHz}^{1/2} \text{ W}^{-1}$ due to the commonly used planar device structure^{60,61}. However, photodetector based on the graphene film exhibited excellent responsivity and detectivity of up to 81.3 mA W^{-1} and $1.1 \times 10^{13} \text{ cmHz}^{1/2} \text{ W}^{-1}$ respectively. The exceptional performances of the graphene film photodetector can attribute to two main factors; firstly the enhancement of absorption due to the disordered stacking of graphene within the film and secondly the vertical device structure, which can shorten the diffusion length of carriers. Finally, the broad response spectrum range of between 365 nm and 1200 nm is of paramount important to many applications in the field of optoelectronic, such as solar cell, light-emitting diode and photocatalysis etc.

Methods

Synthesis of graphene by liquid-phase catalytic growth method. Sucrose solution (0.1g/ml) was heated at 200°C until it became brown solution. A precursor solution (0.5g/ml) was prepared by mixing the brown solution with alcohol and deionized water (at 3:1 ratio). Finally, iodine was added to the precursor solution at a mass ratio of 0.05:1. The sucrose and iodine were purchased from Chengdu Kelong Chemical Reagent Co. Ltd and Sinopharm Chemical Reagent Co. Ltd respectively.

Characterization of as-grown graphene and spin-coated graphene film. UV-visible (U-4100) and TEM (Tecnai G2 TF30) characterization were performed on as-grown graphene and graphene film. The preparation process of graphene film for TEM measurement can be found in Supplementary Notes. Elementary composition of the graphene film were studied using XPS (X-ray photoelectron spectroscopy) (PHI VersaProbe II) with AlK α radiation. Uniformity and thickness of the graphene film was measured using Atomic Force Microscopy (AFM) (Seiko SPA-400).

Fabrication and characterization of photodetectors. The liquid-phase graphene solution was spin-coated on a clear ITO at a rotary speed of 2500 rpm for 60 s. The graphene film was then annealed at 600°C with temperature rising over a period of 30 min and kept constant for 60 min under a low pressure (<5.3 Pa) in a horizontal furnace. Next, aluminum electrode, acted as top electrode, was deposited on the solid graphene film by thermal evaporation under vacuum (2.3×10^{-4} Pa). Gold wire was used to provide electrical connection to the cathode (Al) and anode (ITO). *J-V* measurements on the photodetector were performed using Keithley 2400 source meter. Photocurrent measurements from photodetector were carried out at zero bias voltage using spectral responsivity measurement system (DSR100-D30T75).

Declarations

Acknowledgements

This work was supported by National Natural Science Foundation of China (No. 61106098, 51201150, 11374250 and 11864044), and the Key Project of Applied Basic Research of Yunnan Province, China (No. 2012FA003).

Author contributions

Pin Tian performed the liquid-phase catalytic growth of graphene and prepared the photodetector. Shouzhang Yuan, Dengquan Yang, carried out the photoelectric response measurement and analyzed the data. Libin Tang, Jinzhong Xiang and Kar Seng Teng conceived the project. All authors participated in the discussion and contributed to the manuscript.

Additional information

Supplementary Information accompanies this paper at xxxx

Competing interests: The authors declare no competing financial interests

Reprints and permission information is available online at xxxx

Publisher's note: Springer Nature remains neutral with regard to jurisdictional claims in published maps and institutional affiliations.

References

1. Novoselov, K. S. et al., Electric field effect in atomically thin carbon films. *Science* **306**, 666-669 (2004).
2. Georgiou, T. et al., Vertical field-effect transistor based on graphene-WS₂ heterostructures for flexible and transparent electronics. *Nat. Nanotechnol.* **8**, 100-103 (2013).
3. Schurig, D. et al., Metamaterial electromagnetic cloak at microwave frequencies. *Science* **314**, 977-980 (2006).
4. Park, H. J. et al., Fluid-dynamics-processed highly stretchable, conductive, and printable graphene inks for real-time monitoring sweat during stretching exercise. *Adv. Funct. Mater.* 2011059 (2021).
5. Jang, H. et al., Graphene-Based flexible and stretchable electronics. *Adv. Mater.* **28**, 4184-4202 (2016).
6. Tsikriteas, Z. M., Roscow, J. I., Bowen, C. R. & Khanbareh, H., Flexible ferroelectric wearable devices for medical applications. *iScience* **24**, 101987 (2021).
7. Chae, S. H. et al., Transferred wrinkled Al₂O₃ for highly stretchable and transparent graphene–carbon nanotube transistors. *Nat. Mater.* **12**, 403-409 (2013).
8. An, B. W., Heo, S., Ji, S., Bien, F. & Park, J., Transparent and flexible fingerprint sensor array with multiplexed detection of tactile pressure and skin temperature. *Nat. Commun.* **9**, (2018).
9. Malischewski, M., Adelhardt, M., Sutter, J., Meyer, K. & Seppelt, K., Isolation and structural and electronic characterization of salts of the decamethylferrocene dication. *Science* **353**, 678-682 (2016).
10. Kang, J. H. et al., Cu/graphene hybrid transparent conducting electrodes for organic photovoltaic devices. *Carbon* **171**, 341-349 (2021).
11. Park, I. et al., Flexible and transparent graphene electrode architecture with selective defect decoration for organic Light-Emitting diodes. *Adv. Funct. Mater.* **28**, 1704435 (2018).
12. Park, D. et al., Electrical neural stimulation and simultaneous in vivo monitoring with transparent graphene electrode arrays implanted in GCaMP6f mice. *ACS Nano* **12**, 148-157 (2018).
13. Lee, S. J. et al., Long-term air-stable Au doping of graphene by layer-by-layer assembly with graphene oxide for flexible transparent electrodes. *Carbon* **126**, 241-246 (2018).
14. Gan, X. et al., Chip-integrated ultrafast graphene photodetector with high responsivity. *Nat. Photonics* **7**, 883-887 (2013).

15. Massicotte, M. et al., Picosecond photoresponse in van der waals heterostructures. *Nat. Nanotechnol.* **11**, 42-46 (2016).
16. Koppens, F. H. L. et al., Photodetectors based on graphene, other two-dimensional materials and hybrid systems. *Nat. Nanotechnol.* **9**, 780-793 (2014).
17. Qiu, Q. & Huang, Z., Photodetectors of 2D materials from ultraviolet to terahertz waves. *Adv. Mater.* **33**, 2008126 (2021).
18. Chen, S., Jiang, K., Lou, Z., Chen, D. & Shen, G., Recent developments in graphene-based tactile sensors and E-Skins. *Adv. Mater. Technol.* **3**, 1700248 (2018).
19. Kim, H. & Ahn, J., Graphene for flexible and wearable device applications. *Carbon* **120**, 244-257 (2017).
20. Xu, H. et al., A multifunctional wearable sensor based on a graphene/inverse opal cellulose film for simultaneous, in situ monitoring of human motion and sweat. *Nanoscale* **10**, 2090-2098 (2018).
21. Nair, R. R. et al., Fine structure constant defines visual transparency of graphene. *Science* **320**, 1308 (2008).
22. Bolotin, K. I. et al., Ultrahigh electron mobility in suspended graphene. *Solid State Commun.* **146**, 351-355 (2008).
23. Balandin, A. A. et al., Superior thermal conductivity of single-layer graphene. *Nano Lett.* **8**, 902-907 (2008).
24. Zhou, K. G. et al., Electrically controlled water permeation through graphene oxide membranes. *Nature* **559**, 236-240 (2018).
25. Singh, S. P., Li, Y., Zhang, J., Tour, J. M. & Arnusch, C. J., Sulfur-doped laser-induced porous graphene derived from polysulfone-Class polymers and membranes. *ACS Nano* **12**, 289-297 (2018).
26. Sun, H. et al., Three-dimensional holey-graphene/niobia composite architectures for ultrahigh-rate energy storage. *Science* **356**, 599-604 (2017).
27. Fornasini, L. et al., In situ decoration of laser-scribed graphene with TiO₂ nanoparticles for scalable high-performance micro-supercapacitors. *Carbon* **176**, 296-306 (2021).
28. Park, C. W. et al., Graphene collage on Ni-rich layered oxide cathodes for advanced lithium-ion batteries. *Nat. Commun.* **12**, (2021).
29. Bonaccorso, F. et al., Graphene, related two-dimensional crystals, and hybrid systems for energy conversion and storage. *Science* **347**, 1246501 (2015).
30. Wang, H. et al., Graphene-wrapped sulfur particles as a rechargeable lithium–sulfur battery cathode material with high capacity and cycling stability. *Nano Lett.* **11**, 2644-2647 (2011).
31. Chen, J. et al., Layer-by-layer assembly of vertically conducting graphene devices. *Nat. Commun.* **4**, (2013).
32. Yi, L. et al., Giant energy absorption capacity of graphene-based carbon honeycombs. *Carbon* **118**, 348-357 (2017).

33. Reina, A. et al., Large area, Few-layer graphene films on arbitrary substrates by chemical vapor deposition. *Nano Lett.* **9**, 30-35 (2009).
34. Li, X. et al., Large-area synthesis of high-quality and uniform graphene films on copper foils. *Science* **324**, 1312-1314 (2009).
35. Lee, E. et al., Direct growth of highly stable patterned graphene on dielectric insulators using a surface-adhered solid carbon source. *Adv. Mater.* **30**, 1706569 (2018).
36. Li, B. et al., Orientation-dependent strain relaxation and chemical functionalization of graphene on a Cu(111) foil. *Adv. Mater.* **30**, 1706504 (2018).
37. Subramanian, S. et al, Properties of synthetic epitaxial graphene/molybdenum disulfide lateral heterostructures. *Carbon* **125**, 551-556 (2017).
38. Konstantin, V. E. et al, Towards wafer-size graphene layers by atmospheric pressure graphitization of silicon carbide. *Nat. Mater.* **8**, 203-207 (2009).
39. Samik, M. et al, Growth and luminescence of polytypic InP on epitaxial graphene. *Adv. Funct. Mater.* **28**, 1705592 (2018).
40. Chen, C. et al., Electrical probing of submicroliter liquid using graphene strip transistors built on a nanopipette. *Small* **8**, 43-46 (2012).
41. Ravula S., Baker S. N., Kamath G. & Baker G. A.. Ionic liquid-assisted exfoliation and dispersion: stripping graphene and its two-dimensional layered inorganic counterparts of their inhibitions. *Nanoscale* **7**, 4338–4353 (2015).
42. Tang, L. et al., Preparation, structure, and electrochemical properties of reduced graphene sheet films. *Adv. Funct. Mater.* **19**, 2782-2789 (2009).
43. Cai, J. et al., Atomically precise bottom-up fabrication of graphene nanoribbons. *Nature* **466**, 470-473 (2010).
44. Denk, R. et al., Exciton-dominated optical response of ultra-narrow graphene nanoribbons. *Nat. Commun.* **5**, 4253 (2014).
45. Tang, L. et al., Bottom-up synthesis of large-scale graphene oxide nanosheets. *J. Mater. Chem.* **22**, 5676 (2012).
46. Lai, S. K., Tang, L., Hui, Y. Y., Luk, C. M. & Lau, S. P., A deep ultraviolet to near-infrared photoresponse from glucose-derived graphene oxide. *J. Mater. Chem. C* **2**, 6971-6977 (2014).
47. Wu, Q., Lee, J., Sun, J., Song & Y. J., In situ direct growth of graphene/hexagonal boron nitride heterostructure on SiO₂ substrate without metal catalyst. *Carbon* **138**, 76-80 (2018).
48. Kim, J., Sakakita, H. & Itagaki, H., Low-temperature graphene growth by forced convection of plasma-excited radicals. *Nano Lett.* **19**, 739–746 (2019).
49. Bo, Z. et al, Plasma-enhanced chemical vapor deposition synthesis of vertically oriented graphene nanosheets. *Nanoscale* **5**, 5180-5204 (2013).
50. Narita, A., Wang, X.-Y., Feng, X. & Müllen, K., New advances in nanographene chemistry. *Chem. Soc. Rev.* **44**, 6616-6643 (2015).

51. Fischer, F. R., Bottom-up synthesis of graphene nanoribbons on surfaces. *Adv. Polym. Sci.* **278**, 33-66 (2017).
52. Pham, V. P., Jang, H. S., Whang, D. & Choi, J. Y., Direct growth of graphene on rigid and flexible substrates: progress, applications, and challenges. *Chem. Soc. Rev.* **46**, 6276-6300 (2017).
53. Matassa, R. et al., Characterization of carbon structures produced by graphene self-assembly. *J. Appl. Crystallogr.* **47**, 222-227 (2014).
54. Xu, W. et al., Controllable n-type doping on CVD-grown single- and double-layer graphene mixture. *Adv. Mater.* **27**, 1619–1623 (2015).
55. Xu, X. et al., Interfacial engineering in graphene bandgap. *Chem. Soc. Rev.* **47**, 3059-3099 (2018).
56. Ouyang, F. et al., Bandgap opening/closing of graphene antidot lattices with zigzag-edged hexagonal holes. *Phys. Chem. Chem. Phys.* **16**, 20524-20531 (2014).
57. Gong, X. et al., High-detectivity polymer photodetectors with spectral response from 300 nm to 1450 nm. *Science* **325**, 1665-1667 (2009).
58. Li, J. et al., Metamaterial grating-integrated graphene photodetector with broadband high responsivity. *Appl. Surf. Sci.* **473**, 633–640 (2019).
59. Liu, C.-H., Chang, Y.-C., Norris, T. B. & Zhong, Z., Graphene photodetectors with ultra-broadband and high responsivity at room temperature. *Nat. Nanotechnol.* **9**, 273-278 (2014).
60. Tian, P., Tang, L., Teng, K. S., Xiang, J. & Lau, S. P., Recent advances in graphene homogeneous p–n junction for optoelectronics. *Adv. Mater. Technol.* 1900007 (2019).
61. Wang, G. et al., Seamless lateral graphene p–n junctions formed by selective in situ doping for high-performance photodetectors. *Nat. Commun.* **9**, 5168 (2018).

Figures

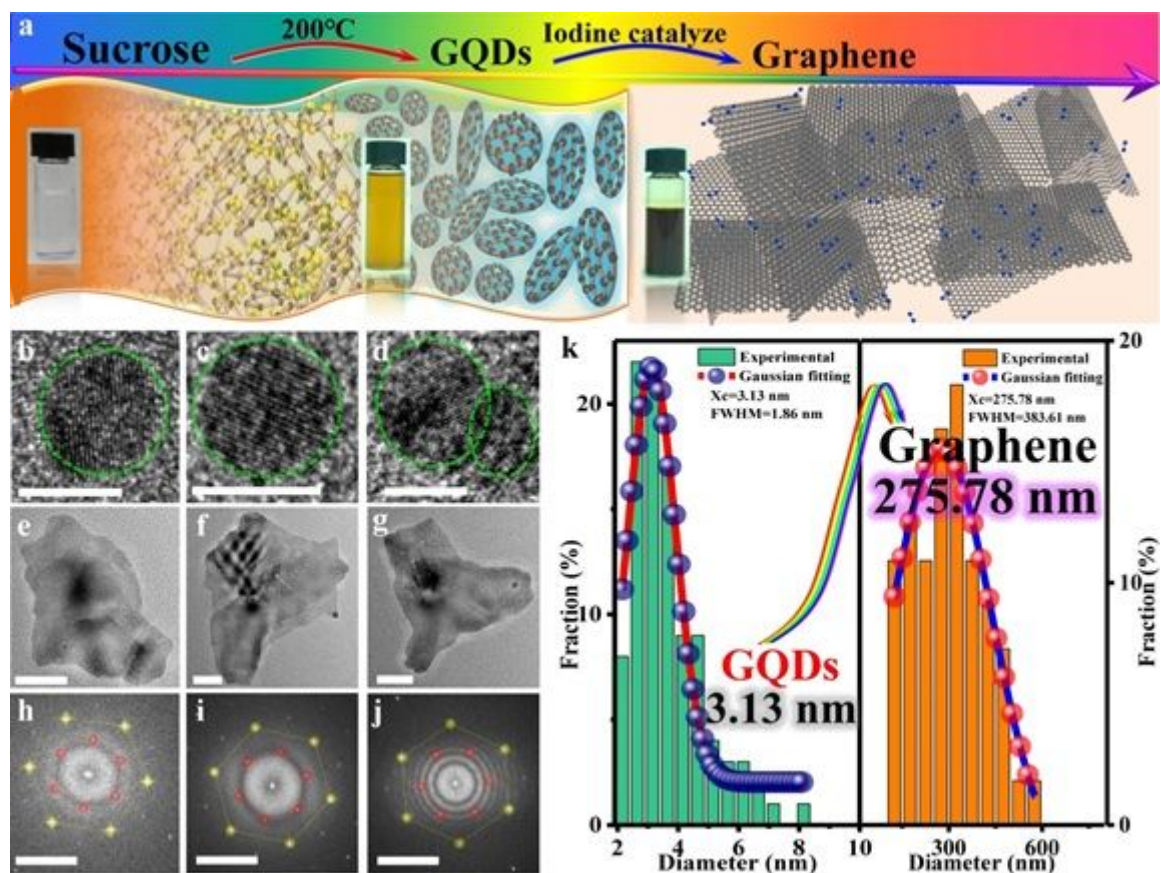


Figure 1

Liquid phase catalytic growth of graphene and TEM characterization. a Schematic diagram illustrating the liquid phase catalytic growth process of graphene. Sucrose solution (left) was annealed at 200°C and turned from colorless to yellow solution, which consisted of solution containing GQDs (middle). Iodine, acting as catalyst (represented as blue molecules in the diagram on the right), was added in to the GQDs solution and turned the solution into dark brown (right), which consisted of the liquid-phase catalyzed graphene. b-d High resolution TEM image of GQDs (scale bar, 5 nm). e-j TEM image of graphene flakes produced by the liquid-phase catalytic method (scale bar, 50 nm). h-j Fast Fourier transform (FFT) patterns of figure e, f and g, respectively (scale bar, 5 1/nm). k Size distribution of the GQDs (left) and graphene (right) prepared by the liquid-phase catalysis method. The statistical size of GQDs and graphene are 3.13 nm and 275.78 nm, respectively.

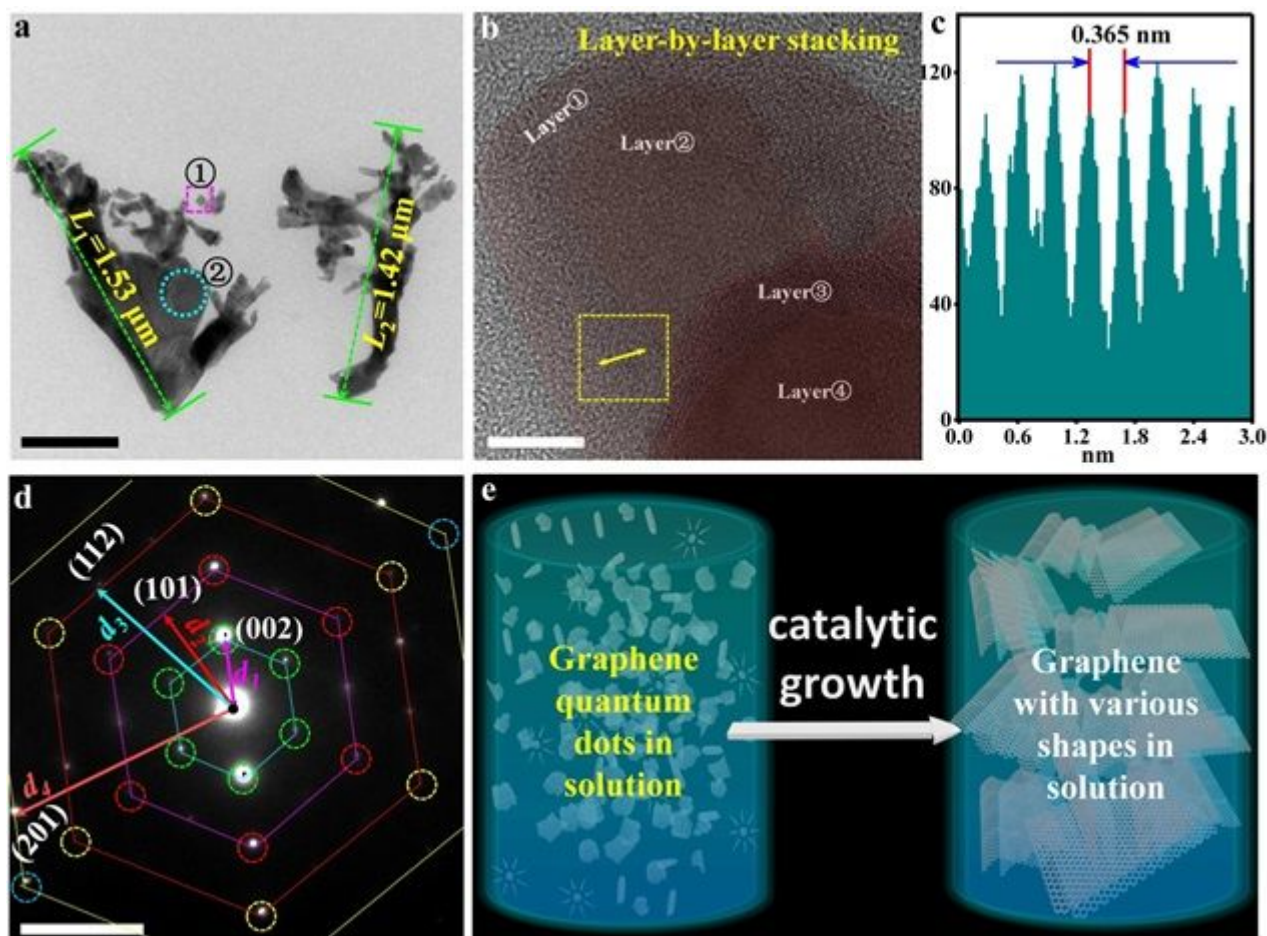


Figure 2

Structural and elemental characterization of graphene prepared by liquid-phase catalytic method. a TEM image of liquid-phase catalytic graphene with size of up to micron scale (scale bar, 500 nm). b High-resolution TEM image of region \square in Fig. a. It revealed the layer-by-layer stacking structure of the liquid-catalyzed graphene. The image showed one, two, three and four layers of graphene (labelled as Layer \square , \square , \square and \square respectively) (scale bar, 10 nm). c Line profile of the yellow rectangular region in Fig. b. An interlayer spacing of 0.365 nm was observed at the layered structure. d Selected area electron diffraction (SAED) pattern of region \square in Fig. a (scale bar, 5 $1/\text{nm}$). d1, d2, d3 and d4 are the distances between the center point and the hexagonal vertex of electron diffraction, which indicate the lattice faces of several vertices, such as (002), (101), (112) and (201), respectively. e Schematic diagram illustrating the growth of graphene from GQDs solution catalyzed using iodine to form various morphologies of graphene flakes via the liquid-phase catalytic growth method.

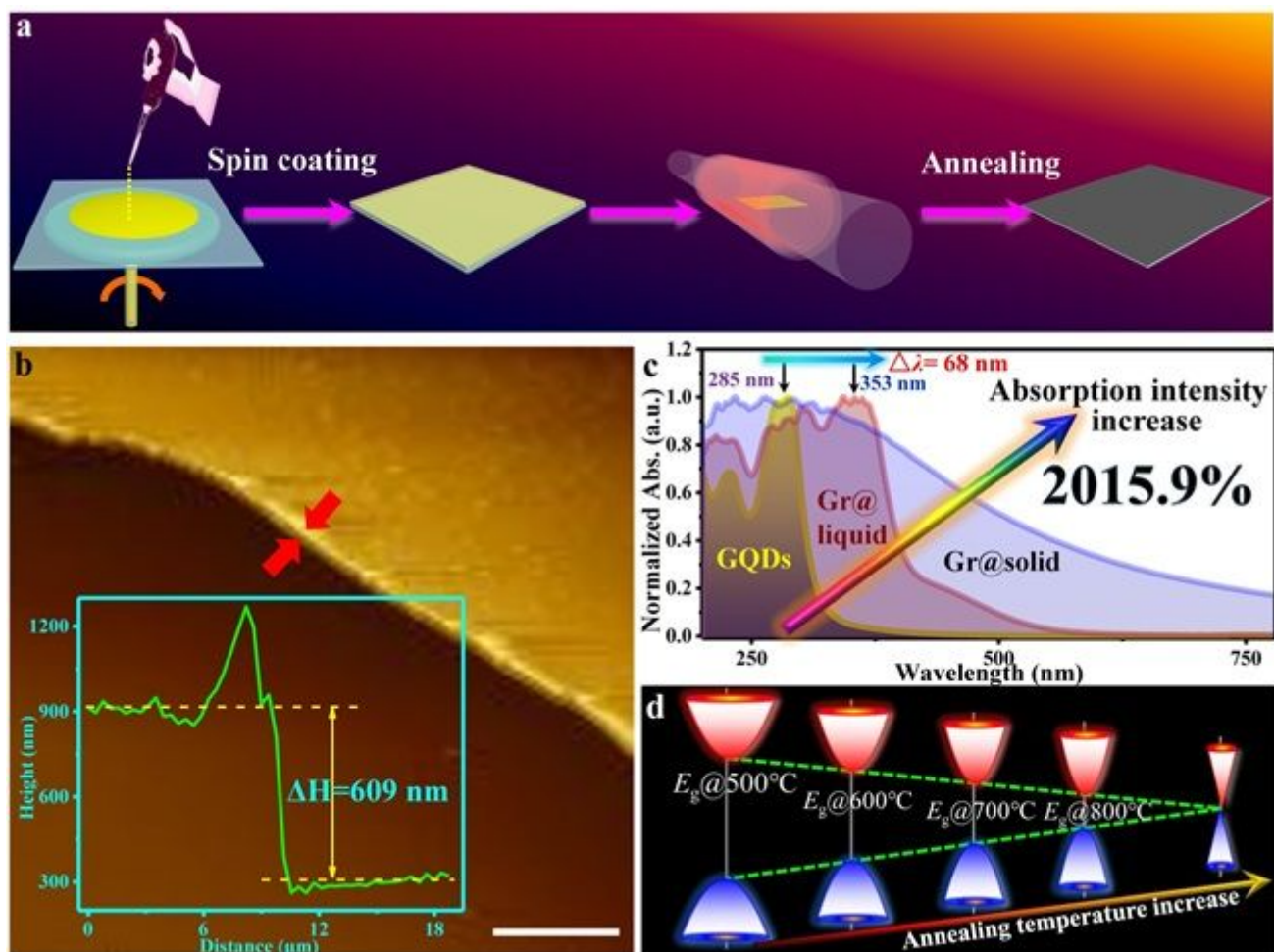


Figure 3

Preparation and characterization of solid graphene film, and its energy gap modulation. a Schematic diagram on the preparation process of solid graphene films. b AFM image of solid graphene films. Inset shows line profile taken across the red arrows. The measured thickness of the film was 609 nm (scale bar, 10 μm). c Normalized UV-visible-infrared spectroscopy measurements of GQDs, liquid graphene solution (Gr@liquid) and solid graphene films (Gr@solid). Red-shift of 68 nm in the absorption peaks of GQDs (285 nm) was observed after catalyzed to form graphene (353 nm). Intensity of absorption was increased by 2015.9% from the GQDs and after the liquid graphene was spin-coated and annealed to form solid graphene film. Further widening of the absorption spectrum was observed on the graphene film. d Schematic diagram showing optical bandgap modulation of solid graphene films at different annealing temperatures. The solid graphene films has an optical bandgap E_g of 2.20 eV , 1.78 eV , 0.77 eV and 0.67 eV when annealed at 500°C, 600°C, 700 °C and 800°C respectively.

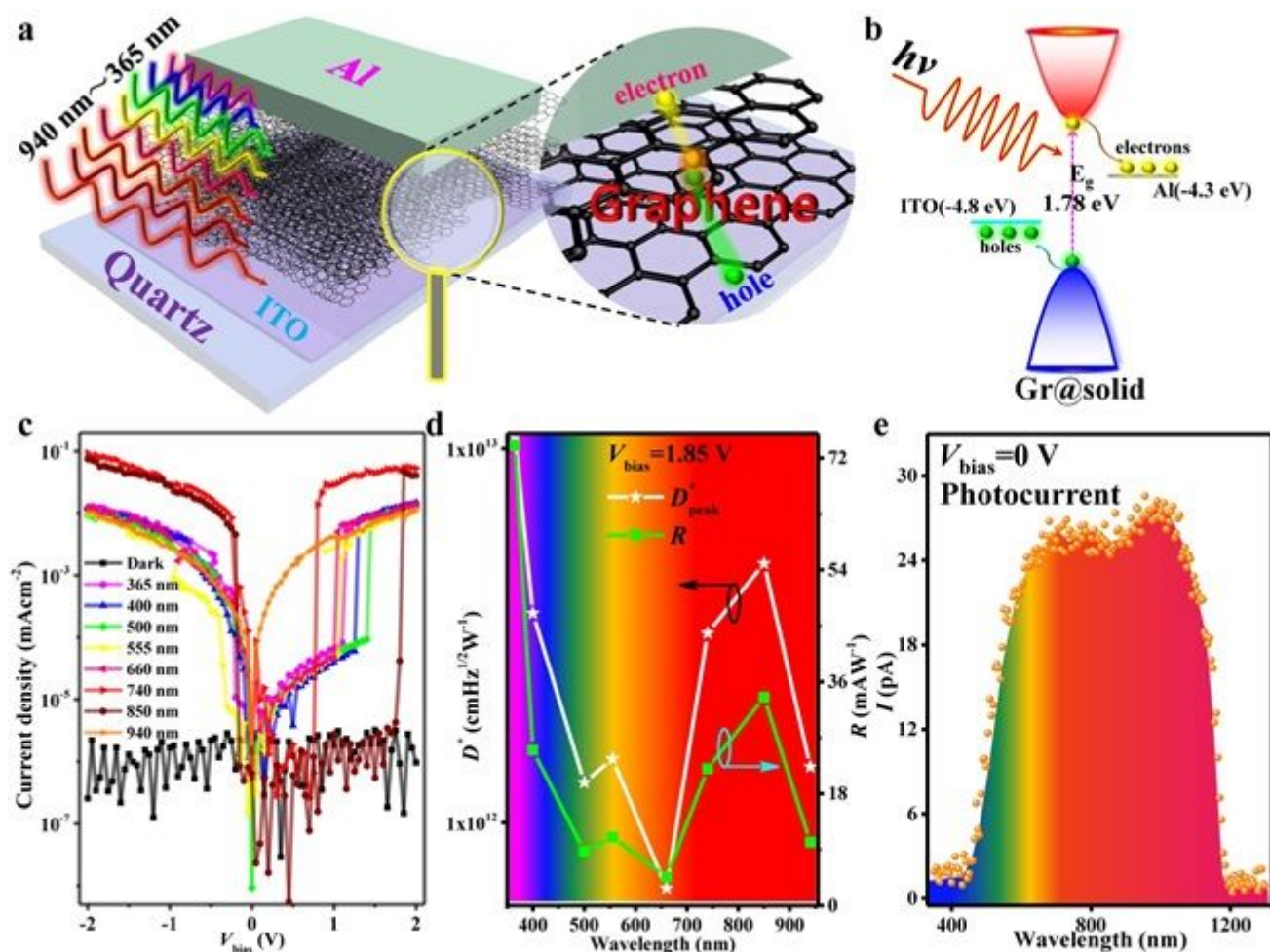


Figure 4

Structure and characterization of a photodetector based on liquid-phase catalytic growth of graphene. a Schematic diagrams of the photodetector (left), and an enlarged diagram (right) of the active layer, which the exciton is produced by induced light and separated into electron and hole. b Energy band of the active layer consisting of the graphene film. c I-V characteristic of the photodetector under dark and illumination of LEDs with different wavelength ranging from 365 nm to 940 nm at various power density. d The peak detectivity and responsivity of photodetector with an applied voltage of 1.85 V at different wavelength. e The photocurrent spectrum of the photodetector without bias voltage, which has a broad response wavelength between 400 nm and 1200 nm.

Supplementary Files

This is a list of supplementary files associated with this preprint. Click to download.

- [Supplementarypictures.pptx](#)
- [NatureCommunicationsSupplementarypaperXXXXXXtp1VT4.docx](#)